Research Paper

Drained instability analysis of sand under biaxial loading using a 3D material model

CrossMark

Mousumi Mukherjee [a], Anurag Gupta [b], Amit Prashant [c,*]

[a] Civil Engineering, Indian Institute of Technology Kanpur, India
[b] Mechanical Engineering, Indian Institute of Technology Kanpur, India
[c] Civil Engineering, Indian Institute of Technology Gandhinagar, India

ABSTRACT

The diffused and localized instabilities in sand under drained biaxial loading have been analyzed here following a plane strain bifurcation framework, where the rate independent material is defined using a generalized 3D non-associative constitutive model. This study is focused on how various instability modes emerge with respect to initial density, confining pressure, and the applied boundary conditions. Results from large deformation framework have been compared with those from small deformation approximation and the later is noticed to fail in capturing the emergence of diffused modes and predicts delayed onset of localization. The theoretical predictions compares well with existing experimental observations.

© 2016 Elsevier Ltd. All rights reserved.

1. Introduction

Soil samples, initially undergoing uniform deformation during laboratory experiments, may experience non-uniform plastic deformation beyond certain state of stress and strain. This state is marked as the onset of plastic instability and acts as precursor to failure. Plastic instabilities may appear in the form of two-phase instability, bulging, buckling, or shear bands due to strain localization [1–6]. Instabilities, either diffused or localized, can emerge in any engineering system depending on the initial and boundary conditions of the domain under consideration. For engineering systems, localized instabilities are a cause of higher concern as they lead to catastrophic failure. However, such localized modes can emerge directly or evolve from other diffused instability modes with continued deformation. In the later case, the localization phenomena can get influenced significantly by the preceding diffused modes. This is the main motivation behind the present study.

In case of saturated sands under drained condition, shear banding is one of the most commonly observed instability modes that arises during triaxial or biaxial experiments as reported in the previous literature [7–13]. Experimental observations revealed that in

comparison to triaxial compression, sand samples are more susceptible to localization in biaxial compression experiments [14–16]. Localization onset and shear band orientation in such tests had significant influence of confining pressure [17,18]. Through a series of experiments on Hostun RF and Manche sand, Desrues and Hammad [17] observed that localization gets significantly delayed with increase in confining pressure or decrease in density. Antisymmetric diffused modes (i.e., buckling) were encountered only in the experiments on loose sands at high confining pressure. However, in all the cases localization was the final instability mode. This type of diffused instability modes are different from the diffused failures characterized by a sudden collapse of the material [19,20].

Instability modes from a uniform states of stress and strain can be assessed theoretically using bifurcation based instability analysis. A bifurcation based instability prediction helps in understanding the initiation of various possible instability modes which can be further useful during modeling of complex geotechnical engineering systems [21–23]. Hill and Hutchinson [24] presented a bifurcation based analytical framework for exploring various non-unique deformation modes that can emerge from a uniform shear-free stress and strain fields during tensile testing of incompressible solids under plane strain condition. Young [25] extended this study to compressive loading and Needleman [26], Vardoulakis [27,1], Chau and Rudnicki [28] further incorporated non-associativity and compressibility in the formulation. However,

the bifurcation problem in these cases were solved only for a set of initial values of state variables instead of considering, the evolution of these state variables with continued deformation. Hence the predicted instability trends were limited to that parameter set. The successive emergence of various instability modes can only be predicted by considering the evolving response of the solid or variation in the magnitude of the state variables with continued deformation. A more general analytical approach in this regard was presented by Bardet [3]. A Mohr–Coulomb type yield surface was used with Rowe's dilatancy based plastic potential. However, such simple model cannot explain the variations observed in the instability modes during experiments and a better representation of stress–strain relation is required for predicting instability modes at different stress states.

The experimental and theoretical understanding of instabilities in sand, as available in the literature, is mainly built on the simple plane strain material models. However, a generalized pressure dependent 3D constitutive model with hardening is expected to predict instability behavior more closely to the experimental observations. This will also provide insights for different instability modes. Previously, Gajo et al. [29,30] employed a 3D constitutive model and small deformation formulation to predict localization onset and post localization behavior of sand in drained biaxial test at varying initial density and confining pressure. They assumed such localized modes to evolve from a homogeneous stress–strain state. It will be interesting to see how other possible diffused modes can emerge and how do they compare with the onset of localized modes, and that is the motivation of present study. Further, it is of interest to identify the influence of small deformation versus large deformation formulation on drained instability predictions. Mukherjee et al. [31] employed a similar pressure dependent 3D constitutive model to examine emergence of localized and liquefaction type solid–fluid instability modes in sand under undrained biaxial loading condition. Such undrained instability modes were noticed to get influenced significantly by the material state and boundary conditions.

The present analysis attempts to assess various drained instability modes in sand that are possible under different densities, confining pressures and the applied boundary conditions during biaxial test. The instability analysis has been posed as a plane strain bifurcation problem from a uniform stress–strain state that follows a rate-independent framework of a generalized 3D non-associative constitutive model. The biaxial condition is simulated for both rigid and mixed boundary conditions with displacement controlled and stress controlled lateral loading, respectively. It is first analyzed with large deformation formulation and then simplified to small deformations. Possible emergence of different diffused modes, i.e., both antisymmetric and symmetric bifurcated modes along with localized shear bands, is analyzed at different states of material and boundary conditions. Influence of loading condition on drained localized modes has been examined by comparing the onset shear strain and shear band angle from biaxial and true triaxial tests with varying intermediate principal stress ratio.

2. Plane strain bifurcation analysis

2.1. Material model

The material behavior is characterized by the following incremental elasto-plastic stress–strain relation [32,33]

$$\overset{\triangledown}{\tau}_{ij} = C_{ijkl} D_{kl}, \tag{1}$$

where $\overset{\triangledown}{\tau}$ is the Jaumann rate of Kirchhoff stress, $\boldsymbol{D}$ is the rate of deformation tensor and C_{ijkl} is a fourth order tensor representing the elasto-plastic tangent stiffness of the material

$$C_{ijkl} = E_{ijkl} - \frac{E_{ijmn} P_{mn} Q_{rs} E_{rskl}}{H + Q_{ab} E_{abcd} P_{cd}}, \tag{2}$$

E_{ijkl} is the isotropic elastic stiffness tensor given by

$$E_{ijkl} = \mu(\delta_{ik}\delta_{jl} + \delta_{il}\delta_{jk}) + \lambda\delta_{ij}\delta_{kl}, \tag{3}$$

μ and λ are the Lamé constants, δ_{ij} is the Kronecker delta, H is the hardening modulus, $\boldsymbol{P}$ and $\boldsymbol{Q}$ are the directions of outer normal to the plastic potential (g) and yield surface (f), respectively

$$P_{ij} = \frac{\partial g}{\partial \tau_{ij}}, \quad Q_{ij} = \frac{\partial f}{\partial \tau_{ij}}. \tag{4}$$

Some other representations of stress rates also exist in the literature, e.g., convective rate, Truesdell rate, Cotter-Rivlin rate, Green–McInnis rate etc. [34,35]; however, Jaumann rate is the most commonly used stress rate for analyzing instability of soil under biaxial shearing [27,1,3,5]. Following Bardet [3], Jaumann rate of Kirchhoff stress has been adopted in the present work. Unlike Mohr–Coulomb model, a generalized 3D constitutive model can account for evolution of the intermediate principal stress under plane strain condition. The 3D constitutive model proposed by Wood [36] has been employed in this study. It is a non-associative model based on critical state concept which includes both shear and volumetric hardening and incorporates the effect of both density and confining pressure. The yield surface (f) and plastic potential (g) are defined by

$$f(\boldsymbol{\tau}, \varepsilon_q^p, \varepsilon_v^p) = \sqrt{3J_2} + \eta_y \frac{I_1'}{3} = 0, \tag{5}$$

$$g(\boldsymbol{\tau}) = \sqrt{3J_2} + M_c \frac{I_1'}{3} \ln \frac{3P_r'}{I_1'}. \tag{6}$$

In the above expressions, ε_q^p and ε_v^p are the shear and volumetric components of logarithmic plastic strain tensor, I_1' is first invariant of Kirchhoff stress tensor, J_2 is second invariant of deviatoric Kirchhoff stress tensor, M_c is the slope of the critical state line in $\sqrt{3J_2}$ versus $-I_1'/3$ plane, P_r' is the intercept of plastic potential on the $I_1'/3$ axis, η_y is shear stress ratio $(-3\sqrt{3J_2}/I_1')$ which is taken as a state variable and controls the evolution of hardening modulus (H)

$$H = -\frac{\partial f}{\partial \eta_y} \frac{\partial \eta_y}{\partial \varepsilon_{ij}^p}^T \frac{\partial g}{\partial \tau_{ij}}. \tag{7}$$

Evolution of the η_y is related to accumulated plastic shear strain ε_q^p by the following hyperbolic function

$$\frac{\eta_y}{\eta_p} = \frac{\varepsilon_q^p}{a + \varepsilon_q^p}, \tag{8}$$

where a is a constant and η_p is peak shear stress ratio. Here, η_p is defined as a function of another state variable ψ which includes information of density or specific volume (v_e) and mean stress,

$$\eta_p = M_c - \kappa\psi = M_c - \kappa[v_e - \varGamma + \varLambda \ln(-I_1'/3)], \tag{9}$$

where, κ is a material constant, $\varLambda$ is slope of the critical state line in compression plane, and $\varGamma$ is intercept of the critical state line on the specific volume axis at mean pressure level of 1 kPa.

2.2. Large deformation formulation

The mathematical framework for plane strain bifurcation analysis of solids has been presented in detail by Hill and Hutchinson [24], Vardoulakis [1], and Bardet [3]. The governing equations for such a bifurcation based instability analysis are presented briefly in Appendix A. Two types of boundary conditions are considered for the biaxially loaded drained sand sample (Fig. 1), namely mixed
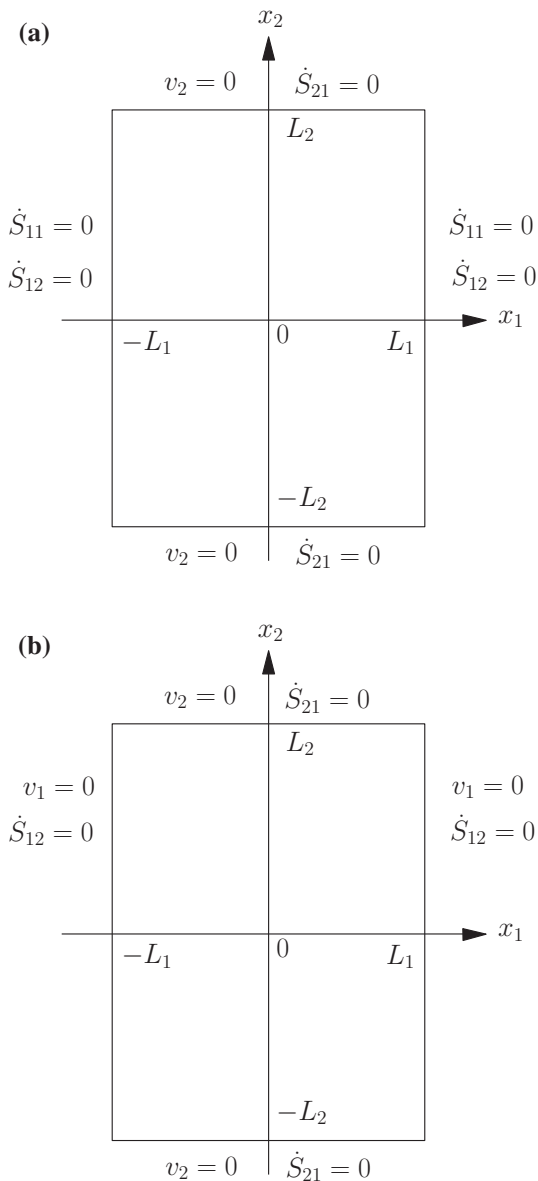
(a)

(b)

Fig. 1. Boundary conditions imposed on the perturbed solutions for performing plane strain bifurcation analysis with (a) mixed boundary and (b) rigid boundary.

boundary and rigid boundary, while assuming no shear stresses acting on any of the boundaries. In the first case, as shown in Fig. 1(a), the top and bottom ($x_2 = \pm L_2$) of soil sample are given constant velocity in x_2 direction and the lateral surfaces are subjected to constant stress σ_{11}. In the second case (Fig. 1(b)), the sample is subjected to constant velocities in both x_1 and x_2 direction at the boundaries $x_1 = \pm L_1$ and $x_2 = \pm L_2$, respectively. Initially a homogeneous stress–strain field prevails during loading; however, at some loading stage, a nonhomogeneous stress–strain rate field may emerge satisfying the same equilibrium and boundary conditions as that for homogeneous stress–strain field. The bifurcation analysis comprises of identifying a non-trivial perturbed solution, i.e., the difference between the nonhomogeneous and homogeneous fields of strain rate. The perturbed solution should satisfy the following boundary conditions:

Case-1

$$\dot{S}_{11} = d_1 v_{1,1} + d_7 v_{2,2} = 0, \quad \dot{S}_{12} = d_4 v_{1,2} + d_5 v_{2,1} = 0 \text{ at } x_1$$
$$= \pm L_1 \quad \text{and} \quad -L_2 \leqslant x_2 \leqslant L_2$$

$$v_2 = 0, \quad \dot{S}_{21} = d_3 v_{1,2} + d_4 v_{2,1} = 0 \text{ at } x_2 = \pm L_2 \quad \text{and}$$
$$-L_1 \leqslant x_1 \leqslant L_1, \tag{10}$$

Case-2

$$v_1 = 0, \quad \dot{S}_{12} = d_4 v_{1,2} + d_5 v_{2,1} = 0, \text{ at } x_1 = \pm L_1 \quad \text{and}$$
$$-L_2 \leqslant x_2 \leqslant L_2$$

$$v_2 = 0, \quad \dot{S}_{21} = d_3 v_{1,2} + d_4 v_{2,1} = 0, \text{ at } x_2 = \pm L_2 \quad \text{and}$$
$$-L_1 \leqslant x_1 \leqslant L_1. \tag{11}$$

During biaxial compression test with mixed boundary, a pressure is imposed on the vertical edges of the samples. Such pressure on the lateral boundary is generally modeled as follower type loading. However, in the present scenario, where bifurcation is assumed to emerge from a rectilinear homogeneous deformation field, the rotation of lateral boundaries is insignificant (resulting in a fixed normal to the boundary). The pressure exerted on the lateral boundaries can therefore be modeled as a dead force acting as normal traction. The onset of bifurcation is identified assuming an infinitesimal transition from the homogeneous field and the assumed perturbed velocity field should further satisfy the same boundary conditions as is the homogeneous deformation field. A similar approach was taken by Vardoulakis [1] and Bardet [3] in their analysis to model the stresses on lateral boundaries.

The possibility of diffused instability modes is investigated, for the boundary conditions considered in Eqs. (10) and (11), by satisfying the stress rate equilibrium equation given in (31). The bifurcated velocity fields corresponding to the diffused instability modes for these two boundary conditions are presented in Appendix B. The velocity field for case-1 (stress controlled) is given by (33) which satisfies (10) and follows the characteristic Eq. (37). There exist three possible solution regimes (EI, EC, P and H) for this characteristic equation and the emergence conditions for these different type of solutions are listed in Appendix B. Whereas, the bifurcated velocity field for case-2 (displacement controlled) satisfies the boundary condition (11) and has the form given in (38). The solution of the characteristic equation for this case exists only in the hyperbolic regime. In the hyperbolic regime, however, the localized modes remain in competition with the diffused instability modes, and both emerge simultaneously as the condition in (36) is met. Such localized modes and their onset conditions are discussed in the Appendix Section C. Since localized modes can develop independent of the boundary conditions, such modes can emerge under both the cases considered in this analysis.

2.3. Simplification with the assumption of small deformation

The previous relations are modified here assuming small deformation, rotational components in the stress rate are thereby neglected. In that case the 1st Piola–Kirchhoff, Cauchy and Kirchhoff stress tensors will be identical and the stress rate equilibrium Eq. (29) can be written as

$$\dot{\sigma}_{11,1} + \dot{\sigma}_{21,2} = 0$$
$$\dot{\sigma}_{12,1} + \dot{\sigma}_{22,2} = 0. \tag{12}$$

The strain tensor ϵ, related to the displacement vector $\boldsymbol{u}$ as $\epsilon_{ij} = \frac{1}{2}(u_{i,j} + u_{j,i})$, satisfies the plane strain kinematic constraint $\dot{\epsilon}_{33} = \dot{\epsilon}_{13} = \dot{\epsilon}_{23} = 0$. The constitutive relation is defined by

$$\dot{\sigma}_{ij} = C_{ijkl}\dot{\epsilon}_{kl}. \tag{13}$$

The governing equations for instability analysis derived in (31) are now replaced by the following relations

$$d_1\dot{u}_{1,11} + d_3\dot{u}_{1,22} + (d_4 + d_7)\dot{u}_{2,12} = 0$$
$$d_5\dot{u}_{2,11} + d_2\dot{u}_{2,22} + (d_4 + d_8)\dot{u}_{1,12} = 0, \tag{14}$$

where the coefficients in the above equation are redefined as

$$d_1 = C_{1111}, \quad d_2 = C_{2222}, \quad d_7 = C_{1122}, \quad d_8 = C_{2211}$$
$$d_3 = d_4 = d_5 = d_6 = C_{1212}. \tag{15}$$

The boundary conditions for the loading cases considered in Section 2.2, with the assumption of small deformation, can be represented as

Case-1

$$\dot{\sigma}_{11} = 0, \quad \dot{\sigma}_{12} = 0 \text{ at } x_1 = \pm L_1 \quad \text{and} \quad -L_2 \leqslant x_2 \leqslant L_2$$
$$\dot{u}_2 = 0, \quad \dot{\sigma}_{21} = 0 \text{ at } x_2 = \pm L_2 \quad \text{and} \quad -L_1 \leqslant x_1 \leqslant L_1, \tag{16}$$

Case-2

$$\dot{u}_1 = 0, \quad \dot{\sigma}_{12} = 0, \text{ at } x_1 = \pm L_1 \quad \text{and} \quad -L_2 \leqslant x_2 \leqslant L_2$$
$$\dot{u}_2 = 0, \quad \dot{\sigma}_{21} = 0, \text{ at } x_2 = \pm L_2 \quad \text{and} \quad -L_1 \leqslant x_1 \leqslant L_1. \tag{17}$$

For case-1, the expression of perturbed displacement rates for diffused instabilities under small deformation can be represented as

$$\dot{u}_1(x_1, x_2) = \dot{u}_1(x_1)\cos{(\beta x_2 + \theta_2)}$$
$$\dot{u}_2(x_1, x_2) = \dot{u}_2(x_1)\sin{(\beta x_2 + \theta_2)}, \tag{18}$$

where $\dot{u}_1(x_1) = Ae^{i\alpha x_1}$

$$\dot{u}_2(x_1) = Be^{i\alpha x_1}.$$

Substituting (18) into (13), a system of algebraic equation can be formed in terms of the variable $Z = \alpha/\beta$

$$(d_1 Z^2 + d_3)A - (d_4 + d_7)iZB = 0$$
$$(d_4 + d_8)iZA + (d_5 Z^2 + d_2)B = 0. \tag{19}$$

Nontrivial solutions for A and B are obtained only when the determinant of coefficients in (19) is equal to zero, which gives the characteristic equation of (36), but the coefficients are now calculated using (15). The initiation conditions for such instability modes can be obtained from Table 5 using these modified coefficients. Similar simplifications also hold for case-2; however, the perturbed displacement rates for this case take the form

$$\dot{u}_1(x_1, x_2) = \dot{U}_1\sin(\beta_1 x_1 + \theta_1)\cos{(\beta x_2 + \theta_2)}$$
$$\dot{u}_2(x_1, x_2) = \dot{U}_2\cos(\beta_1 x_1 + \theta_1)\sin{(\beta x_2 + \theta_2)}. \tag{20}$$

The emergence of diffused modes for case-2 is checked from Table 5 only in the hyperbolic regime.

The localization analysis with small deformation assumption is similar to the one explained in Section C. The difference in the strain rate field inside and outside the shear band should satisfy the condition, $[\![\dot{\epsilon}_{ij}]\!] = \frac{1}{2}(g_i n_j + g_j n_i)$ to maintain kinematic compatibility. Whereas, the stress rate equilibrium across the shear band enforces the condition $n_j[\![\dot{\sigma}_{ji}]\!] = 0$. The symbol $[\![\cdot]\!]$ denotes the jump or difference in magnitude of the corresponding field variable within and outside the band. Plane strain constraint in this case is ensured by $[\![\dot{\epsilon}_{33}]\!] = [\![\dot{\epsilon}_{13}]\!] = [\![\dot{\epsilon}_{23}]\!] = 0$, which further results $g_3 = n_3 = 0$. These conditions again lead to the characteristic equation identical to the diffused bifurcation case. The real roots can be calculated at hyperbolic and parabolic regime from Table 5 with modified expressions of a_1, b_1 and c_1 from Eqs. (37) and (15).

## 3. Properties of material considered for instability analysis

Drained biaxial test simulations are carried out for sand (Hostun sand RF) considering different density states with initial void ratio (e_0) varying from 0.65 to 0.9 and different confining pressures

Table 1
Material constants considered in the analysis [42,36].

Parameter	Description	Value
μ	Shear modulus	$G_0/3$
v	Poisson's ratio	0.1
M_c	Slope of critical state line in $\sqrt{(3J_2)}$–$(-I_1'/3)$ plane	1.2
Λ	Slope of critical state line in specific volume (v_e)–$\ln(-I_1'/3)$ plane	0.03
Γ	Intercept for critical state line in v_e–$\ln(-I_1'/3)$ plane at 1 kPa effective mean pressure	1.969
a	Parameter controlling hyperbolic stiffness relationship	0.0016
κ	Relation between changes in state parameter (ψ) and current peak stress ratio (η_p)	2

ranging from 50 kPa to 400 kPa. The material parameters considered for the analysis are given in Table 1. There exist many expressions in the literature which consider the influence of mean pressure on the elastic stiffness of soil [37–41]. Following Gajo and Wood [42], a pressure dependent elastic tangent stiffness has been employed in the analysis. In this case, the elastic shear modulus μ is related to the dynamic shear modulus G_0 through a scalar factor, where G_0 is function of initial specific volume v_0 and mean effective stress $I_1'/3$ expressed in kPa [43]

$$G_0 = 3230\frac{(3.97 - v_0)^2}{v_0}\sqrt{(-I_1'/3)}. \tag{21}$$
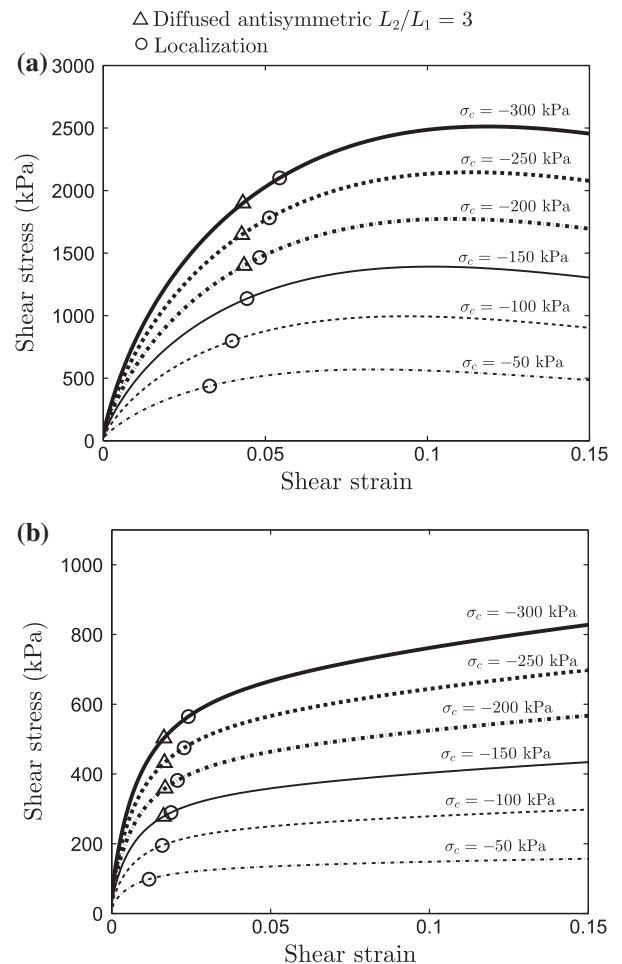
Fig. 2. Predicted stress–strain behavior of sand sample under biaxial loading, at (a) $e_0 = 0.65$ and (b) $e_0 = 0.90$, with varying confining pressure.

The homogeneous stress–strain field for drained biaxial test is obtained by integrating the elasto-plastic constitutive Eqs. (2)–(9) numerically by considering the boundary conditions of Eqs. (10) and (11). A fully explicit return mapping algorithm has been employed for this purpose [44]. In case of large deformation simulations, an objective algorithm based on the notion of rotated configuration has been used in conjunction with the explicit return mapping [45]. However, the homogeneous stress–strain field under plane strain biaxial stretching excludes any rotation, and hence the unrotated and the Jaumann rate of Cauchy stress are identical. As a result, the stress–strain response obtained for small and large deformation problem are similar until bifurcation, i.e., onset of instability.

Typical stress strain behavior and volumetric response at two void ratios 0.65 and 0.9 for confining pressure range 50 to 300 kPa magnitude has been plotted in Figs. 2 and 3 respectively. A general trend of increasing shear stress has been observed with increase in the confining pressure for both the cases of loading boundary. It can be observed that the volumetric response is throughout compressive at $e_0 = 0.9$; whereas it is initially compressive and finally dilative for $e_0 = 0.65$ depending on the level of confining pressure. Moreover, increase in the confining pressure results into an enhanced compressive volumetric response at both 0.65 and 0.9 void ratio. Based on the volumetric response, the sand samples with $e_0 = 0.65$ and 0.9 can be considered as dense and loose, respectively. This can also be confirmed from the critical void ratio (e_c) at any confining pressure, which is calculated from the following condition and listed in Table 2:

$$(1 + e_c) - \Gamma + \Lambda \ln(-I_1'/3) = 0. \tag{22}$$

Fig. 4(a) presents the volumetric behavior at various density states for the confining pressure of 200 kPa. It can be observed that the loose samples with void ratio higher than the critical void ratio exhibit compressive response; whereas the dense ones with lower void ratios shows dilative response. The corresponding stress–strain behavior have been plotted in Fig. 4(b). The dense samples exhibit strain softening response unlike the loose sands which exhibit a continuous strain hardening behavior. This confirms to the sand behavior reported in various triaxial or biaxial experiments of sand samples [9].

4. Instability under large deformation framework

Under large deformation framework, the mixed boundary case can possibly show instability with antisymmetric diffused mode, symmetric diffused mode and localization; whereas only symmetric type of diffused modes and localization can take place for rigid boundary case [1]. Besides depending on density and confinement, the diffused modes are also function of sample geometry, i.e., aspect ratio (L_2/L_1). Present analysis aims only to predict the onset of each of these possible types of instability modes. For each of the test simulations, however, the uniform stress–strain state prediction is valid till emergence of any of such instability modes. Hence, this analysis does not consider identification of gradually evolving multiple instability modes during continued shearing under a given test condition.

As mentioned earlier, the instability onsets are determined here based on the global stability approach [46,24]. Following earlier work of Hill and Raniecki, Bigoni [47,48] has presented a unified framework to study bifurcation and instability in non-associated elastoplastic materials addressing several global and local conditions which ensure uniqueness and stability of the solution. These conditions are essentially based on the concept of linear comparison solid developed by Hill for associative plasticity, and extended to non-associative plasticity by Raniecki [49] & Raniecki and
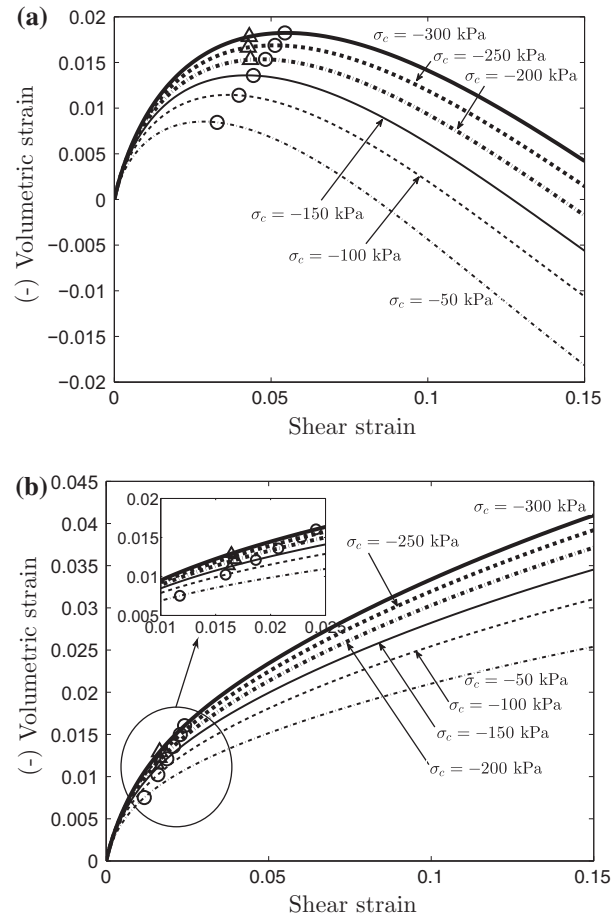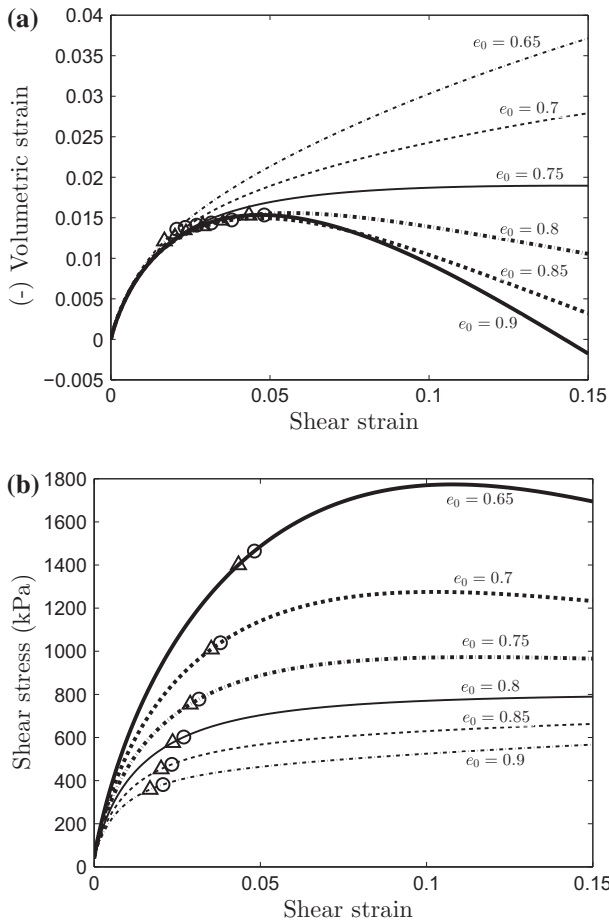

Fig. 3. Predicted volumetric response of sand sample under biaxial loading, at (a) $e_0 = 0.65$ and (b) $e_0 = 0.90$, with varying confining pressure.

Table 2
Critical void ratio at different confining pressure.

Confining pressure (kPa)	Critical void ratio
50	0.851
100	0.83
150	0.818
200	0.81
250	0.803
300	0.798
400	0.789
500	0.783

Bruhns [50]. As emphasized by Bigoni [47], the "in loading comparison solid" (analogous to Hills comparison solid for associative materials) provides only the upper bound for bifurcation. The lower bound is obtained by using an optimal "Raneicki comparison solid". Both of these coincide for associative plasticity. The global criteria of bifurcation can be used to derive several local criteria, namely, (1) positive definiteness (PD) and (2) non-singularity (NS) of constitutive operator, (3) strong ellipticity (SE), (4) ellipticity (E), and (5) flutter (F); see Bigoni [47] for details. Under homogeneous conditions with all-round traction boundary conditions, the failure of PD implies failure of Hill sufficient condition for stability and uniqueness. This is not generally true for non-associative materials where failure of NS of constitutive tensor might be critical for bifurcation [47]. On the other hand, for the dual homogeneous problem with displacements prescribed all over the boundary, it is the failure of SE which leads to bifurcation of solu-

Fig. 4. Predicted (a) volumetric and (b) stress–strain behavior of sand sample under biaxial loading at $\sigma_c = -200$ kPa with density.

instability mode refers to the numeric value of the hardening modulus required to satisfy the equation of emergence of that particular mode. A particular instability mode is triggered only when the critical hardening modulus exceeds the actual hardening modulus (H) for the given stress state. The equation of emergence for antisymmetric diffused mode (Table 5) is solved in EC regime by employing numerical root finding technique (method of bisection). The antisymmetric mode gets activated when H_{diff} exceeds H. Fig. 5 (a) shows evolution of the normalized critical hardening modulus during shearing for void ratio 0.65 at confining pressure 300 kPa. Interestingly, the antisymmetric mode emerged only for the aspect ratio $L_2/L_1 = 3$. Diffused instability modes for this case can also be obtained for aspect ratios, $L_2/L_1 \geqslant 4$. However, the discussions here are restricted only up to $L_2/L_1 = 3$ and results for $L_2/L_1 \geqslant 4$ are not included. The onset of antisymmetric modes associated with different aspect ratios at various density and confinement has been calculated and marked in Figs. 2–4. In case of dense sample ($e_0 = 0.65$), the antisymmetric mode for aspect ratio $L_2/L_1 = 3$ emerges for 200 kPa confining pressure or higher, whereas for loose sample, it gets activated from confining stress level of 150 kPa. For both dense and loose samples, increase of confining pressure favors the initiation of antisymmetric diffused modes. However, once such modes get activated, the onset shear strain for these instabilities remain nearly independent of the level of confinement. It is also observed that the onset shear strain for such modes is sensitive to the density state and it decreases considerably with increase in the void ratio (Fig. 4(b)). Such diffused instability modes are generated in the contractive regime irrespective of what is the density state (Figs. 3 and 4(a)).

As antisymmetric diffused modes are more prone to emerge at loose state or softer conditions, the simulations are repeated with a reduced magnitude of elastic shear modulus ($\mu = G_0/6$) to examine

tions [51]. However, for non-associative materials, SE is usually lost while the acoustic tensor is still non-singular [47]. It is therefore appropriate to decide loss of uniqueness of solution in the non-associative case on the basis of the loss of ellipticity of acoustic tensor. This condition marks the onset of strain localization in elastoplastic solids, which is identical to the condition derived by [24] for localization from a global bifurcation perspective. Hence, for rigid boundary conditions (also known as "generalized van Hove conditions"), global and local bifurcation criteria coincide. In the present analysis with all-round rigid boundary, i.e., for case-2, localization emerges as the initial bifurcation mode from the global stability analysis, which is also identical to Bigoni's local criteria of loss of ellipticity. However for case-1, which is a mixed boundary value problem, it is not very clear how the diffused instability modes can be directly related to the failure of various local criteria.
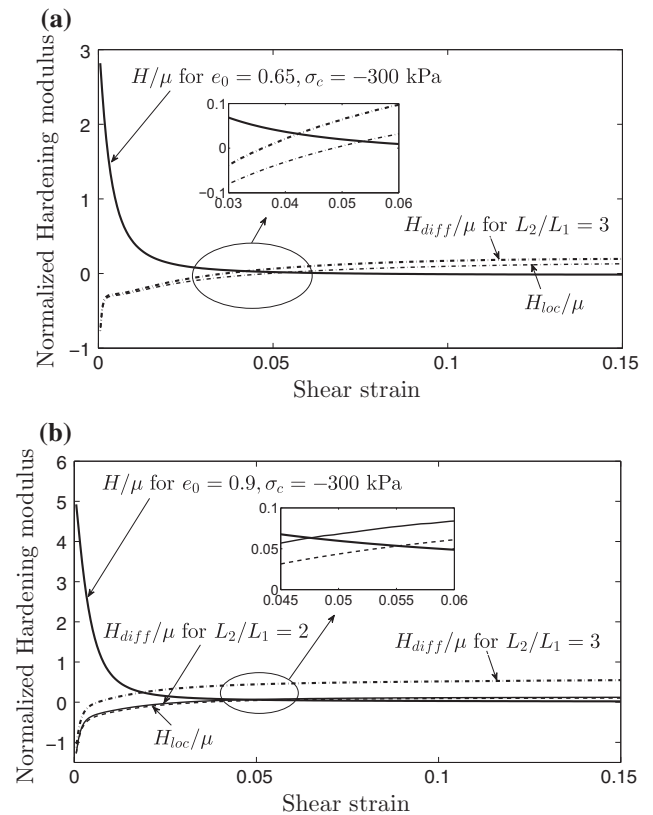
4.1. Mixed boundary case

4.1.1. Antisymmetric modes

Three sets of aspects ratios, $L_2/L_1 = 3, 2,$ and 1, are considered to investigate probability of emergence of fundamental modes ($m = 1$) of antisymmetric diffused instabilities at different density and confinement. For any biaxial loading configuration, simulated at a particular initial density and confinement, the critical hardening modulus for fundamental antisymmetric diffused mode (H_{diff}) is calculated at each stress state for a given aspect ratio. At a given stress state, the critical hardening modulus corresponding to an

Fig. 5. Normalized actual and critical hardening modulus evolution for void ratio (a) 0.65 ($\mu = G_0/3$) and (b) 0.90 ($\mu = G_0/6$) at confining pressure 300 kPa.

the effect of elastic properties on occurrence of such instabilities. Example of evolution of the normalized critical hardening modulus is shown in Fig. 5(b) for the sample with $e_0 = 0.9$ at 300 kPa confining pressure. Unlike the previous case of elastic stiffness, the antisymmetric mode gets activated even for the aspect ratio $L_2/L_1 = 2$ along with $L_2/L_1 = 3$. The stress–strain responses for different combinations of void ratio and confining pressure, with $\mu = G_0/6$, are plotted in Figs. 6 and 7 respectively. Possible antisymmetric diffused bifurcation modes are also marked in these curves. Though the overall stress–strain response remained nearly unaffected, the change in the elastic shear modulus shows its significant influence on the observed instability characteristics. The antisymmetric diffused modes associated with aspect ratio $L_2/L_1 = 3$, emerges at both the density states and at all levels of confinement. However, the range of onset shear strain of such modes are similar to the simulations with $\mu = G_0/3$. Unlike the simulations with $\mu = G_0/3$, the onset shear strains of such instabilities at $L_2/L_1 = 3$ remain nearly independent of the level confinement for loose sand in contrast to the dense samples, where it slightly decreases with increasing confining pressure. On the other hand, the antisymmetric mode is encountered only for loose samples at higher confining pressures during simulations with aspect ratio $L_2/L_1 = 2$. Diffused instability mode emerges at much higher shear strains in case of $L_2/L_1 = 2$ in comparison to that for aspect ratio $L_2/L_1 = 3$. It is clear from these figures that diffused antisymmetric modes are more susceptible to slender samples with higher
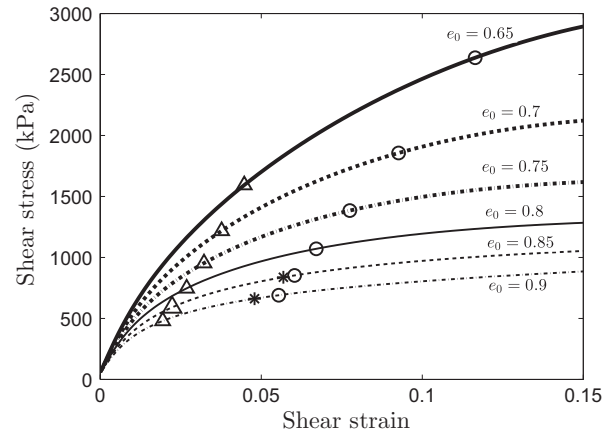

Fig. 7. Predicted stress–strain behavior of sand sample under biaxial loading at 300 kPa confining pressure with varying density state ($\mu = G_0/6$).

aspect ratio. However, they can even emerge for bulky samples at lower densities and higher confinement. These predictions are consistent with the observations reported by the previous researchers. Theoretical study of Vardoulakis [1] and Bardet [3] also revealed that higher aspect ratio favors the emergence of diffused antisymmetric modes. Desrues and Hammad [17] performed series of biaxial experiments to examine instability behavior of sand at different densities and confining level. They noticed diffused antisymmetric instability modes to appear in the biaxial test of loose sample at higher confining pressure. Such antisymmetric diffused mode may appear in the form of buckling and induce non-uniform deformation field, which physically result into non-uniform distribution of void ratio or density field within the sample. In real field condition, antisymmetric diffused instabilities can be expected to emerge at greater depth of soil strata containing loose sand.

4.1.2. Symmetric modes

Possibility of symmetric bifurcation modes has been explored in EC domain. These modes do not develop in the simulations with $\mu = G_0/3$ and $G_0/6$; however, they emerge when shear modulus values are further reduced to $\mu = G_0/8$. Even for such cases, these modes get activated only for high density and high level of confinement. For example, at $e_0 = 0.65$, the symmetric modes start emerging from 400 kPa confining pressure onward and no such modes are observed in case of simulations with $e_0 = 0.9$. Due to pressure dependency of soil, level of confinement has its impact on the elastic modulus which further shows influence on the initiation of various instability modes. The scalar factor related to elastic shear modulus in Table 1 has been varied here to take into account the influence of soil type. At any given confinement, the diffused instability modes are observed to be more susceptible to a lower magnitude of elastic stiffness as per the current finding. This implies diffused instability will initiate for a softer material (e.g., sands with higher percentage of fines) with a similar variation of density and confinement.

Fig. 8(a) presents the critical hardening modulus evolution for symmetric diffused mode at 0.65 void ratio and 400 kPa confining pressure. Unlike antisymmetric mode, the symmetric bifurcation solution presented here is obtained for fundamental mode ($m = 1$) of a bulky sample with aspect ratio $L_2/L_1 = 1$. It can be noticed from (34) that the result associated to the fundamental mode also represents the solution for second symmetric diffused mode ($m = 2$) for a sample with aspect ratio $L_2/L_1 = 2$. Hence, higher symmetric diffused modes can emerge for slender samples at very high confining stress when simulated for higher densities. The stress–strain behavior for this sample ($e_0 = 0.65$ and

△ Diffused antisymmetric $L_2/L_1 = 3$
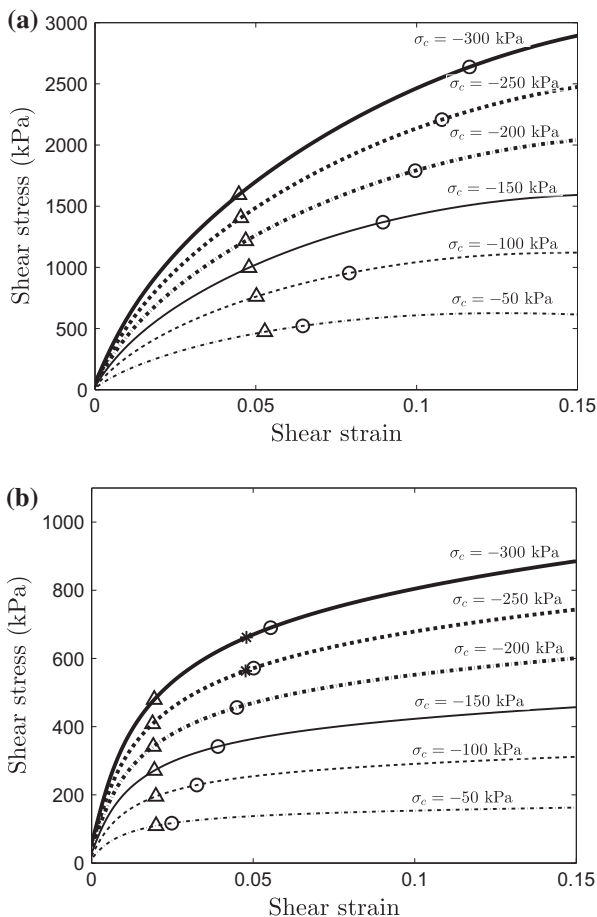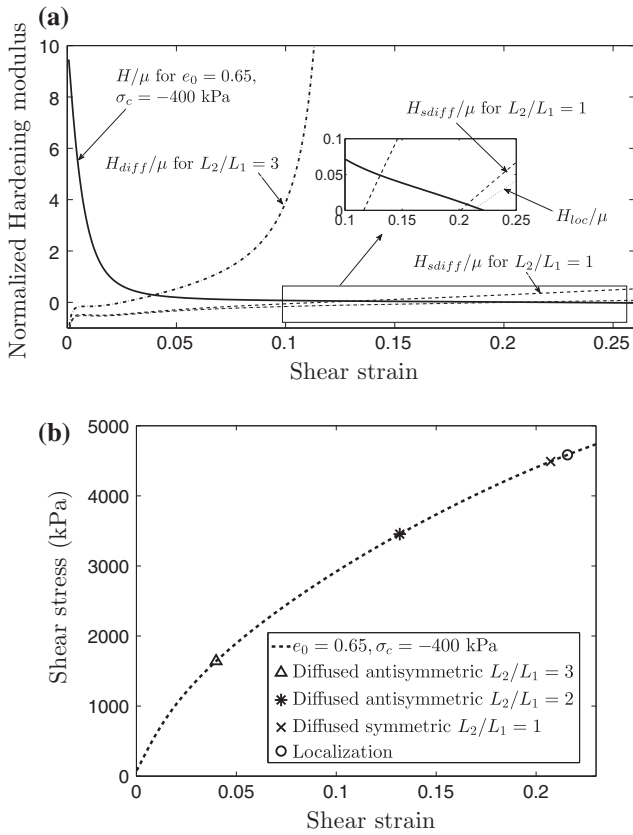✳ Diffused antisymmetric $L_2/L_1 = 2$
○ Localization

Fig. 6. Predicted stress–strain behavior of sand sample under biaxial loading at (a) $e_0 = 0.65$ and (b) $e_0 = 0.90$ with varying confining pressure ($\mu = G_0/6$).

Fig. 8. (a) Normalized critical hardening modulus evolution and (b) predicted stress–strain behavior of sand sample under biaxial loading at the void ratio 0.65 and confining pressure of 400 kPa ($\mu = G_0/8$).

$\sigma_c = -400$ kPa) is plotted in Fig. 8(b) and it is to be noticed that the symmetric modes emerge only at high shear strains, e.g., around 20%. In such cases, the antisymmetric modes ($m = 1$) for slender samples with $L_2/L_1 = 3$ and 2 are already in competition and their emergence criteria are met at much lower shear strains, i.e., around 4 and 13%, respectively. Based on the theoretical study, Vardoulakis [1] also suggested that symmetric diffused modes or bulging type of instability is not common in biaxial tests and can be observed in bulky specimens of dense sand.

4.1.3. Localized modes

The localization onset is identified by comparing the critical hardening modulus for localization (H_{loc}) against the actual hardening modulus (H), as depicted in Fig. 5(a). In this case, H_{loc} is calculated by solving the equation of emergence in hyperbolic regime using the relations from Section C. The onsets of localization for various test simulations have been marked in Figs. 2–8(b). Localization is observed in the hardening regime which is usually found true with the use of non-associative constitutive relation [52]. Localization is found to be more significant at lower confining pressure irrespective of the density state and it gets delayed with increase in the confinement level (Figs. 2 and 6). For slender samples, however, the antisymmetric mode may precede the localization mode in case of higher confining stress at lower density. For any level of confinement, the shear strain at localization increases considerably with decrease in the void ratio (Figs. 4 and 7). Unlike diffused instability modes, the shear strain at localization is much higher for the cases with $\mu = G_0/6$ than that for $\mu = G_0/3$ which is consistent with the observation of Gajo et al. [30]. Similar to the present theoretical predictions, Desrues and Hammad [17] also noticed localization for both loose and dense sand samples during

their experiments. They also observed that increase in the confining pressure retarded the localization onset. Whereas, such increase in the confining pressure resulted in the emergence of diffused antisymmetric mode for loose samples which is consistent with the present study. Shear bands were the final instability modes observed for all of the tests. However, the localization phenomena was observed to get retarded by the decrease in the density level, which could not be captured by the present theoretical study.

Friction and dilatancy angle are two important parameters often used in the previous literatures to determine the onset of different types of instability. The mobilized friction angle (ϕ) is defined in terms of major and minor principal stress; whereas the dilatancy angle (ψ_d) is defined in terms of major and minor principal strain increments [53]. A positive value of ψ_d implies dilatancy while a negative one corresponds to contraction. While analyzing diffused and localization modes, Vardoulakis [27,1] assumed that these two parameters will achieve their peak values at the onset of instability. However, biaxial experiments of Desrues et al. [14] revealed that initiation of localization can take place before the peak in the overall stress–strain curve. The mobilized friction angle and dilatancy angle during shearing are plotted in Fig. 9, at two density states with different confining pressure for the case $\mu = G_0/6$. The instability onsets are also marked in the plots. In all of the cases, instability occurs much before the stage when the stress ratio or dilation angle reaches its peak. Irrespective of the confining pressure and density, the instability emerges in the compressive region indicating negative dilation angle.

4.2. Rigid boundary case

In case of rigid boundaries, instability gets activated just on the Elliptic/Hyperbolic boundary where solution is available for diffused symmetric modes in hyperbolic regime. However, localized modes also emerge simultaneously at this point resulting into a mixed mode of failure. As the homogeneous stress–strain simulation results are same for the mixed and rigid boundary cases, the localization onset marked in Figs. 2–8(b) are the only instability onset points available for the corresponding rigid boundary test configurations. The onset shear strain of localization and the inclination of band angle for two density states with varying confining pressure are plotted in Fig. 10 for the case of $\mu = G_0/6$. At higher densities, the onset shear strain of localization increases more rapidly with the increasing confining pressure. On the other hand, the band orientation angle shows slightly decreasing trend with increase in the confining pressure which is relatively more significant at higher density. Han and Drescher [18] also observed experimentally that for dense sand, the shear strain at onset of localization increases with increase in the confining pressure; whereas, the shear band orientation angle decreases.

Two conventional theories are used in Soil Mechanics to predict the inclination of shear bands (measured clockwise from the minor principal stress direction) for two-dimensional plane strain problems, namely Mohr–Coulomb theory (θ_{CM}) and Roscoe theory (θ_{CR})

$$\theta_{CM} = \frac{\pi}{4} + \frac{\phi}{2} \quad \text{and} \quad \theta_{CR} = \frac{\pi}{4} + \frac{\psi_d}{2}. \tag{23}$$

Bardet [53] showed that (23) gives upper and lower bounds of the theoretically predicted shear band angles. Arthur et al. [54] proposed an empirical formula considering an average of these two values

$$\theta_{CA} = \frac{\pi}{4} + \frac{\phi}{4} + \frac{\psi_d}{4}. \tag{24}$$

The localization angles have been calculated for the void ratios $e_0 = 0.65$ and 0.9 considering the above relations and using the
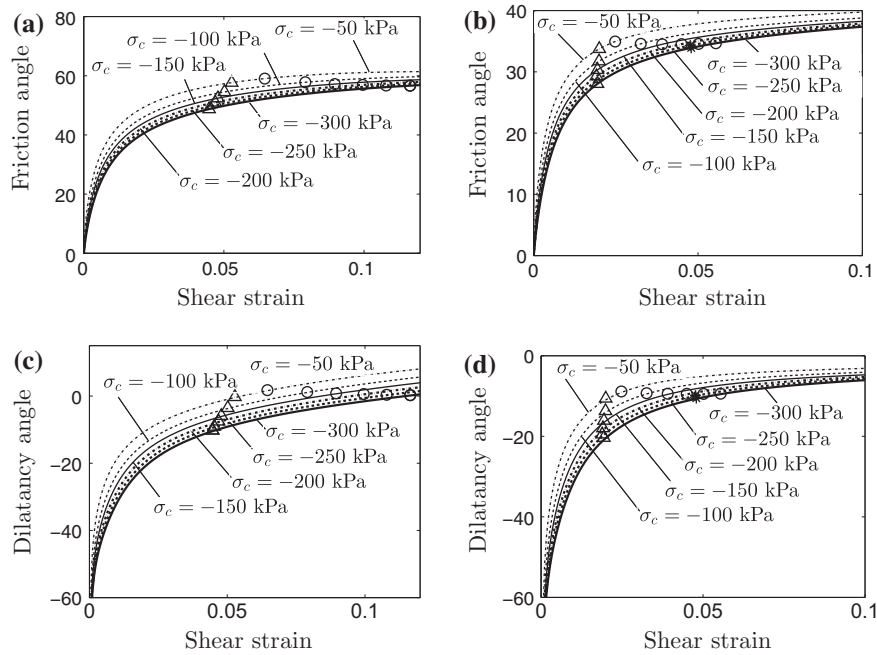
Fig. 9. Evolution of friction angle and dilatancy angle at (a, c) $e_0 = 0.65$ and (b, d) $e_0 = 0.90$ with varying confining pressure for the case $\mu = G_0/6$.
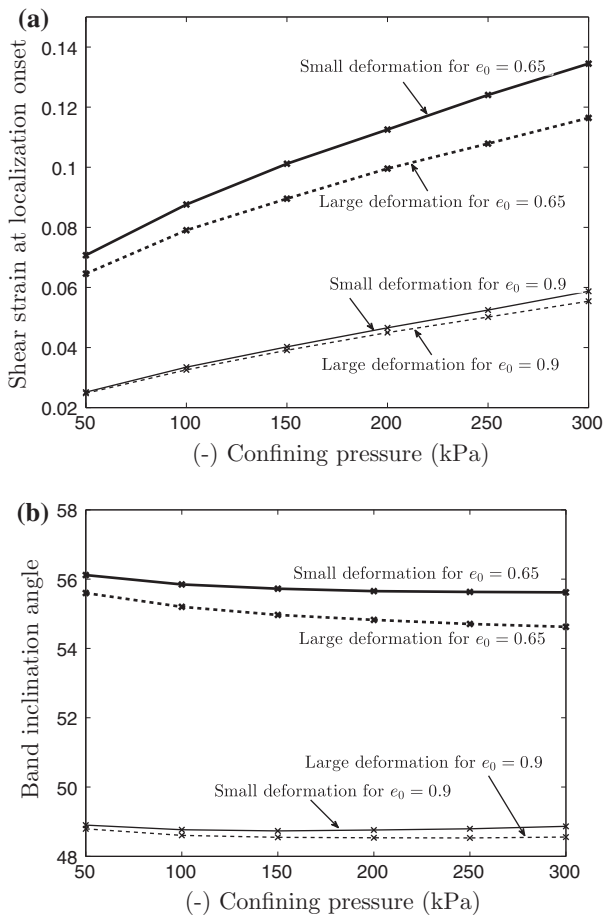
magnitude of friction and dilation angle at the onset of localization. These values are listed in Table 3. For all of the cases, the values of θ_{CM} are higher and θ_{CR} are considerably lower than the values θ_b calculated from the bifurcation analysis. The values of θ_{CA} are also on slightly higher side, but within 3–5 degrees of difference.

5. Instability under small deformation framework

5.1. Instabilities in biaxial test

Different types of instability modes are also examined with the assumption of small deformation by employing the simplification made in the Section 2.3. No diffused modes are captured in this type of analysis and localization is the only instability mode observed irrespective of the boundary type, mixed or rigid. The localization predictions with small deformation assumption are also presented in Fig. 10 in comparison with the large deformation results. The observation regarding the effect of confining pressure and density level on the onset shear strain for localization is similar

Fig. 10. (a) Shear strain and (b) band angle variation with confining pressure for void ratio 0.65 and 0.9 for the case $\mu = G_0/6$.

Table 3
Friction (θ) and dilation angle (ψ_d) at onset of localization, shear band orientation angles calculated from plane strain bifurcation theory (θ_b) and (23) and (24) for sand samples $e_0 = 0.65$ and 0.9 at different confining pressure under large deformation framework.

Void ratio	Confining pressure (compressive)	ϕ	ψ_d	θ_b	θ_{CM}	θ_{CR}	θ_{CA}
$e_0 = 0.65$	50	59.1	1.8	55.6	74.5	45.9	60.2
	100	57.8	1.2	55.2	73.9	45.6	59.8
	150	57.2	0.8	54.9	73.6	45.4	59.5
	200	56.9	0.6	54.8	73.5	45.3	59.4
	250	56.7	0.4	54.7	73.4	45.2	59.3
	300	56.7	0.3	54.6	73.3	45.1	59.2
$e_0 = 0.9$	50	34.9	−8.9	48.8	62.5	40.6	51.5
	100	34.6	−9.3	48.6	62.3	40.4	51.3
	150	34.5	−9.4	48.5	62.3	40.3	51.3
	200	34.5	−9.5	48.5	62.3	40.3	51.3
	250	34.5	−9.5	48.5	62.3	40.3	51.3
	300	34.6	−9.5	48.5	62.3	40.3	51.3

to that of large deformation analysis and comparable with the small strain localization predictions of Gajo et al. [29,30]. However, the magnitude of predicted onset shear strains are comparatively larger in case of small deformation framework. This difference increases for denser samples and higher confining pressures, where the predicted onset shear strain itself is relatively high. In case of loose samples ($e_0 = 0.9$), such variation is within 1.5–5.5%; whereas, for dense samples ($e_0 = 0.65$) the difference can vary from 8.5 to 14% or even higher depending on the level of confining pressure. Hence, a small deformation based localization analysis can lead to delayed prediction of shear band initiation and considerably overpredict the onset shear strain. Small deformation approximation are often assumed while performing conventional geotechnical analysis or design in the range of shear strain level of 5–10%; however, that does not appear to be a good assumption in the context of instability prediction. Delayed instability prediction in such framework will lead to unconservative design with respect to failure of the structure. The band angle variation remains nearly similar under the two frameworks, with slightly higher values for small deformation case, which is more noticeable at higher confining pressure and densities.

5.2. Effect of loading condition on localized instability

Drained true triaxial tests are simulated at different intermediate principal stress ratios to explore the influence of loading condition on the emergence of localization, i.e., onset shear strain and shear band angle. Similar to the plane strain instability case, the 3D instability analysis has been posed as a bifurcation problem from a uniform stress–strain condition and the onset of localization is identified when the acoustic tensor loses its positive definiteness [52,55]. An expression of critical hardening modulus corresponding to localization condition has been derived by Rice [55].

Drained true triaxial and biaxial test simulations are carried out for loose saturated Hostun RF sand specimen with $e_0 = 0.84$ at 300 kPa confining pressure. True triaxial tests are simulated for seven different values (0, 0.25, 0.4, 0.5. 0.75, 0.85 and 0.95) of intermediate principal stress ratio (b), which is defined by

$$b = \frac{\sigma_2 - \sigma_3}{\sigma_1 - \sigma_3}. \tag{25}$$

where, σ_i are the principal stress ratios. The homogeneous stress–strain fields for the drained tests are obtained by integrating the elastoplastic constitutive equations numerically, satisfying the loading boundary conditions. Fig. 11 presents the stress–strain and volumetric behavior under biaxial and true triaxial test configuration ($b = 0, 0.25, 0.4, 0.5, 0.75, 0.8, 0.95$). For any level of shear strain, the shear stress increases continuously with increasing intermediate principal stress ratio. The stress–strain and volumetric behavior under biaxial test simulation is very close to the true triaxial results with $b = 0.5$.

At each stress state, the critical hardening modulus is obtained by numerically solving the maximization problem for the rotation of vector $\hat{\boldsymbol{n}}$. For true triaxial tests, the vector $\hat{\boldsymbol{n}}$ has been initially rotated in three-dimensional stress space and observed that the critical hardening modulus reaches its maximum value only when the second component of $\hat{\boldsymbol{n}}$ is zero. Hence, the critical plane has been observed to be perpendicular to the intermediate principal direction, which is consistent with the previous study [52]. In case of biaxial test, the critical plane for shear banding is calculated following the procedure mentioned in Section 2.3. Fig. 12 presents the comparison between the plastic hardening modulus (H) and critical hardening modulus (H_{cr}) corresponding to the loss of ellipticity for true triaxial tests at different b values. A similar comparison in case of biaxial test has been presented in Fig. 13(a). For cases
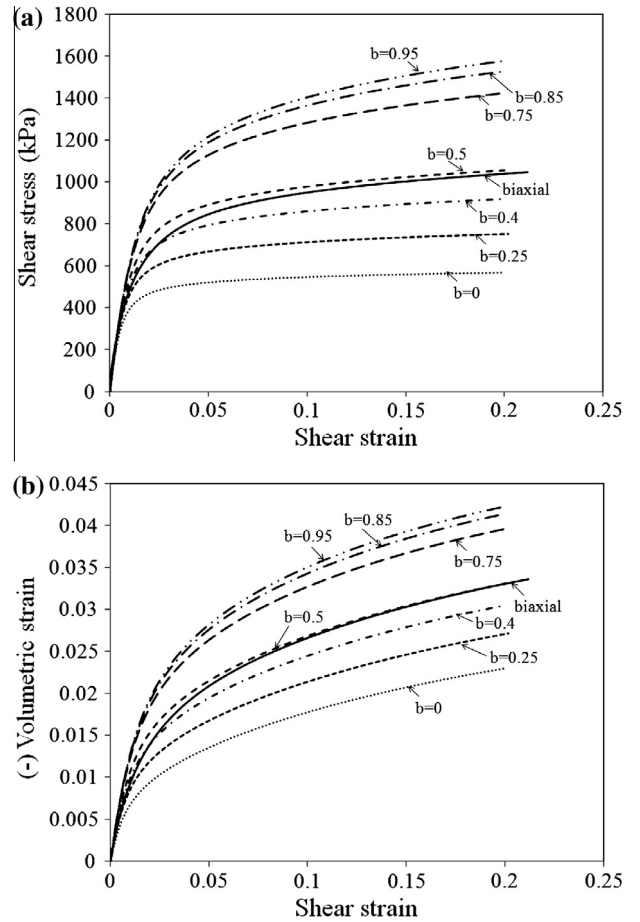

Fig. 11. (a) Stress–strain and (b) volumetric behavior under biaxial and true triaxial test configuration ($b = 0, 0.25, 0.4, 0.5, 0.75, 0.8, 0.95$).

$b < 0.4$, the H_{cr} decreases with increasing shearing and remains significantly lower than the plastic hardening modulus. Whereas, for b values equal or greater than 0.4, H_{cr} increases with the shearing and remains almost constant at a small positive value. Similar type of variation is also observed in the biaxial simulation, where H_{cr} increases with shearing and reaches a positive value (Fig. 13 (a)). The onset of shear band occurs only when H_{cr} exceeds H and it can be observed from Figs. 12 and 13(a) that the localization initiates for biaxial simulation and true tiaxial simulations with b values greater than 0.4. As mentioned earlier, localization occurs in the hardening regime due to consideration of non-associative plasticity [52].

The shear strain at onset of localization and shear band orientation angles are presented in Table 4. The shear band angles are measured with respect to the direction of lateral confining pressure. Though for true triaxial simulations, localization occurs only when b values are equal or greater than 0.4, the onset shear strain for localization initially reduces as b changes from 0.4 to 0.5. Thereafter, the onset strain significantly gets delayed with increasing $b(> 0.5)$ values. The shear band angle is also noticed to increase with increasing value of b. The variation of onset strain and band angle with b values qualitatively match with the experimental observations of Lade and Wang [56], Wang and Lade [57]. They have performed series of drained true triaxial tests on Santa Monica Beach sand at different b values and noticed that the shear bands are more sensitive to initiate at medium range of b values (0.18–0.85).

The variation of b value in biaxial test with continued deformation is plotted in Fig. 13(b). If we ignore the very initial deforma-
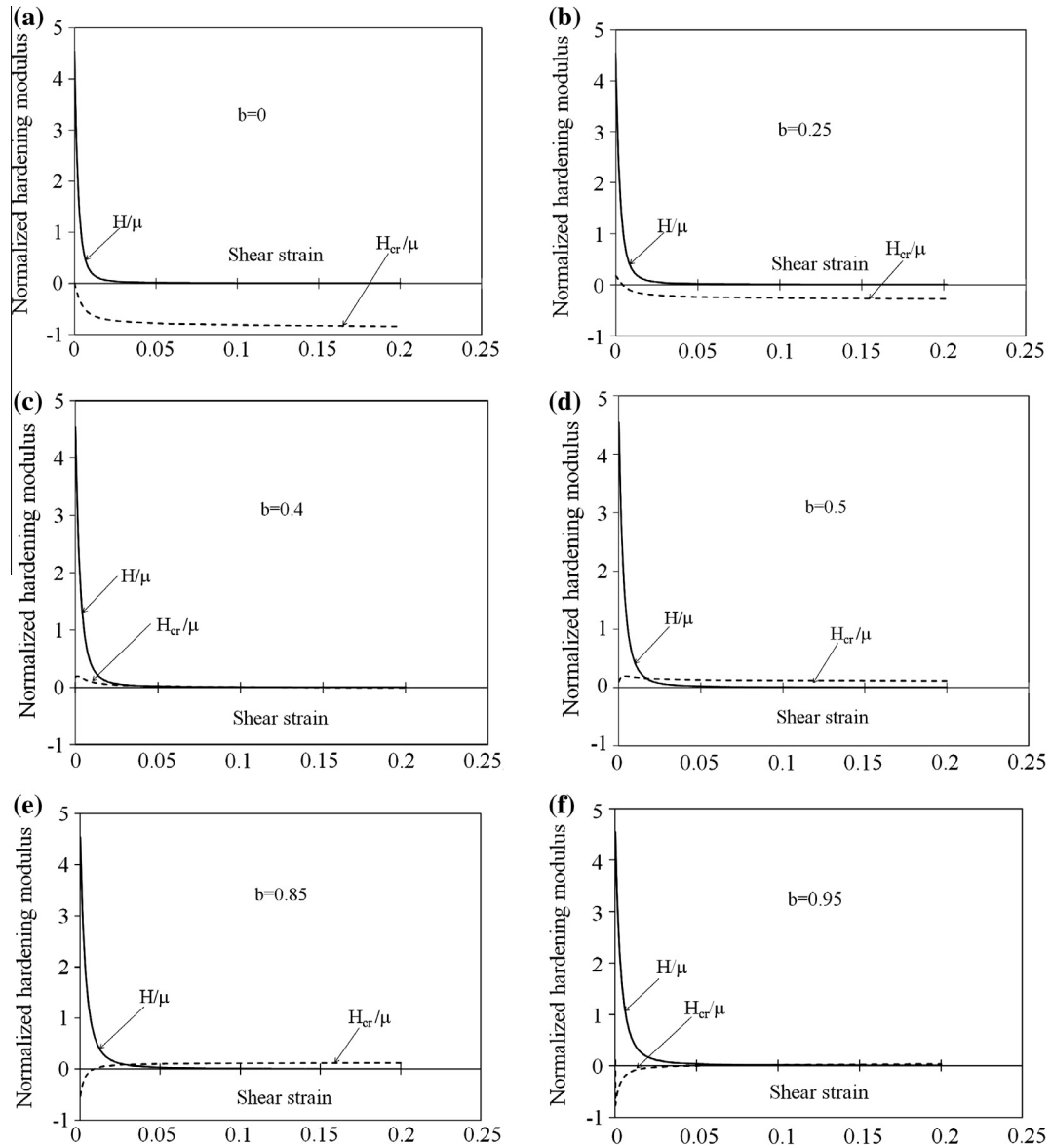
Fig. 12. Variation of plastic hardening modulus and critical hardening modulus from loss of ellipticity condition for true triaxial simulations.
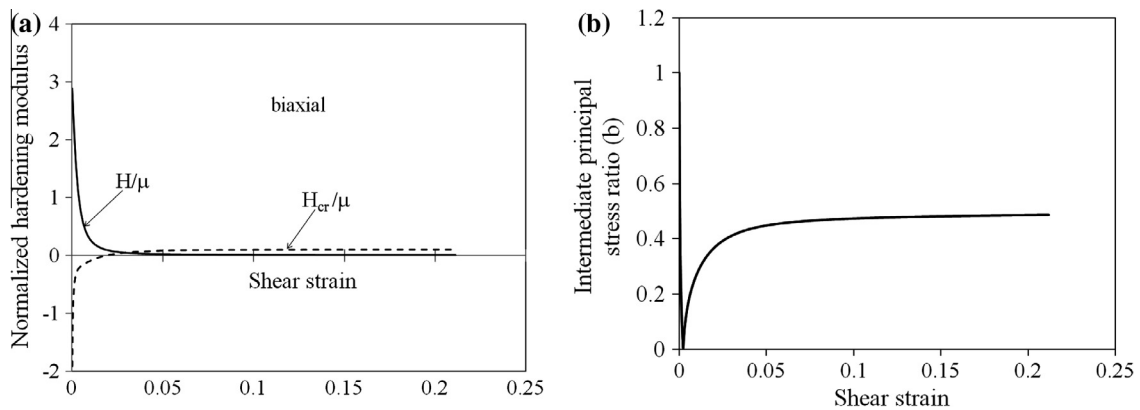

Fig. 13. (a) Variation of plastic hardening modulus and critical hardening modulus and (b) intermediate principal stress ratio in biaxial simulation.

Table 4
Shear strain at onset of localization and shear band orientation angle for biaxial simulation and true triaxial simulations for different b values.

Simulation type		Shear strain at onset of localization	Shear band orientation angle (deg)
True triaxial	$b = 0.40$	0.037	49.3
	$b = 0.50$	0.017	49.7
	$b = 0.75$	0.02	54.1
	$b = 0.85$	0.029	56.5
	$b = 0.95$	0.085	59.7
Biaxial test		0.029	49.2

tion regime, the b value in biaxial test increases from very small positive magnitude to a value nearly equal to 0.5; whereas, the b value near localization falls within the range 0.4–0.5. The onset strain and shear band orientation angle in biaxial test is very similar to that of true triaxial tests with $b = 0.4 - 0.5$, which may be due to the similar stress state observed for these two types of test. This analysis also explains the reason for biaxial tests to exhibit more pronounced localization phenomenon than the conventional axisymmetric triaxial test ($b = 0$) during experiments under compressive loading [14,16].

6. Charts for onset of Instability

The onset shear strains for different types of instabilities are presented using contour plots in Figs. 14 and 15. These results

(a)

(b)
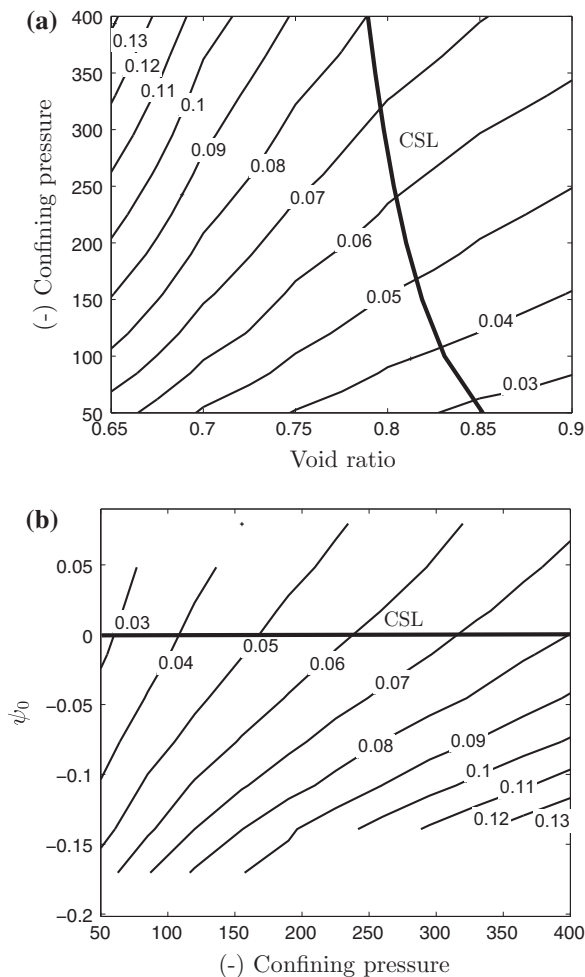
Fig. 14. Contours of onset shear strain at localization with (a) void ratio & confining pressure and (b) ψ_0 & confining pressure for the case $\mu = G_0/6$.

are obtained by varying the initial void ratio from 0.65 to 0.9 and confining pressure over the range 50–400 kPa for the case $\mu = G_0/6$. As a reduced value of shear modulus favors the emergence of various drained instability modes (Section 4.1.1), the value $G_0/6$ has been selected to establish a generalized trend for the onset of such instability modes. The state variable ψ represents relative density of sand in some sense and accounts for the effect of both initial density and confining pressure. It defines the material state with respect to the critical state, where ψ takes a value equal to zero. A negative value of initial state variable (ψ_0) implies denser state with dilative response and positive value stands for loose state with compressive response.

Fig. 14(a) presents the contour of shear strain at localization along with the critical state line (CSL). These contours are found to be nearly perpendicular to the CSL. The onset shear strain level increases with decrease in the void ratio and increasing confinement. Hence, void ratio and confinement both have significant effect on the onset shear strain for localization. This is further verified from Fig. 14(b), where onset shear strains are presented with respect to the confining pressure and ψ_0, and which indicate no unique relation with ψ_0 due to dependence on both void ratio and confining pressure.

Similar analysis is performed for diffused antisymmetric mode at two different aspect ratios $L_2/L_1 = 3$ and 2, for which charts are shown in Fig. 15. Unlike localization, onset of this mode occurs with the strain contours nearly parallel to the CSL line as shown in Fig. 15(a) and (c). Further analysis with respect to ψ_0 and confining pressure in Fig. 15(b) and (d) indicates that the strain contours are nearly independent of confining pressure and depend only on ψ_0. This implies that relative density plays the primary role in influencing the onset shear strain for diffused instability in comparison to confining pressure. Diffused instability predictions then can be made solely based on the parameter ψ_0.

The observations from above discussion have been summarized in the charts shown in Fig. 16 for occurrence of different instability modes. Onset shear strains for localization type of instabilities can be obtained from Fig. 16(a) based on ψ_0 and the confining pressure of the biaxial test. Whereas, onset of diffused instabilities can be predicted from ψ_0 using Fig. 16(b) for a given aspect ratio of the sample. Such charts will be helpful for identification of possible instability modes in biaxial testing depending on the geometry of sample, initial density state and confining pressure. The onset shear strains for different instabilities, predicted from these charts, are limited to the material parameters considered in the simulation. However, similar analogy can be used for understanding the occurrence of different instability modes in the biaxial testing of other soils subjected to a different set of material parameter.

7. Conclusions

This study examines the emergence of various drained instability modes of sand under biaxial loading condition with due consideration to both large and small deformation formulation. Plane strain bifurcation problem is analyzed for a rate independent 3D non-associative constitutive model. Drained diffused instability modes are encountered only for large deformation formulation. Diffused instability modes can lead to localized mode on further shearing, which makes it important to understand and predict reasonably well. Moreover, the small deformation framework overpredicts both the onset strain of localization and band angle in comparison to the large deformation formulation. In case of small deformation formulation, deformation gradient is assumed to be small compared to unity. As a result, geometric linearization can be performed by neglecting the higher order terms while calculating the strain tensors in small deformation framework. However,
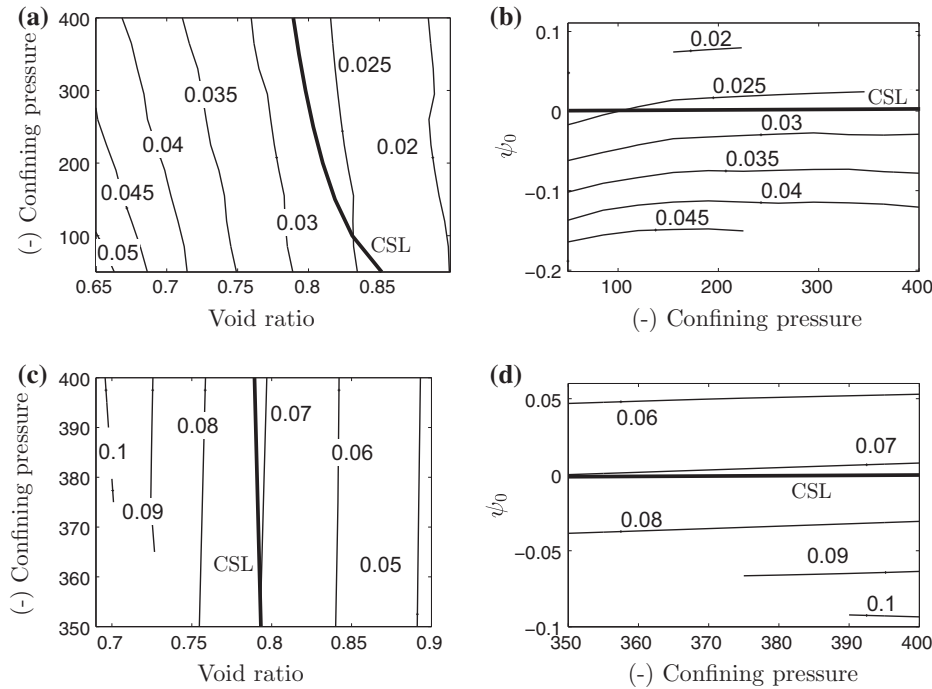
Fig. 15. Contours of shear strain at onset of diffused instability for $L_2/L_1 = 3$ and $L_2/L_1 = 2$ with (a, c) void ratio & confining pressure and (b, d) ψ_0 & confining pressure for the case $\mu = G_0/6$.
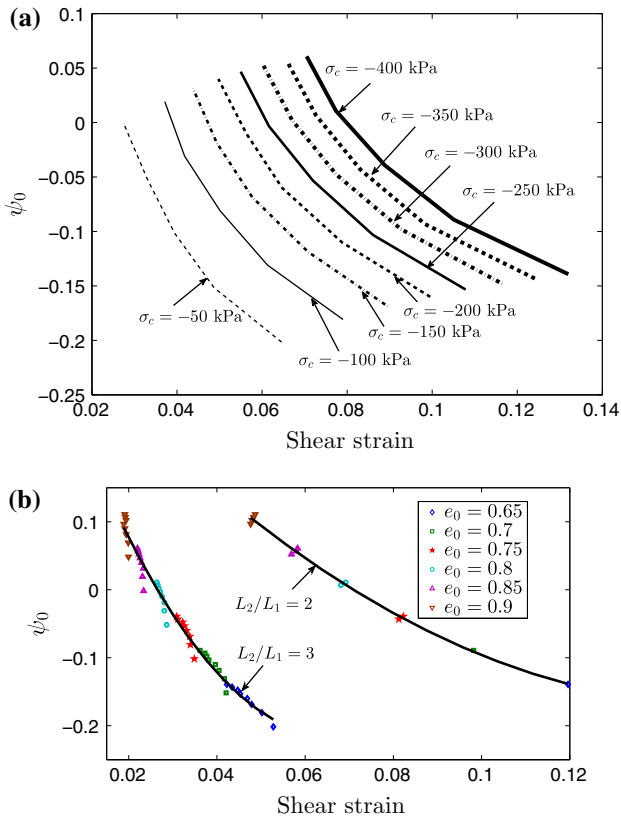

Fig. 16. Charts for predicting onset shear strain for (a) localization, (b) antisymmetric diffused modes with aspect ratio $L_2/L_1 = 3$ and $L_2/L_1 = 2$ considering $\mu = G_0/6$.

such assumptions are not employed in a large deformation framework. In case of shear band formation and diffused localization, the deformation gradients are better represented by including geometric nonlinearity in the formulation and hence, large deformation formulation show early predictions of instability.

Diffused mode emerges only in case of mixed boundary, which is also susceptible to the slenderness ratio of the sample. Previously, Desrues and Hammad [17] observed experimentally that the antisymmetric diffused modes are more prone to emerge in biaxial tests of loose sand samples at higher confining pressures. It is interesting to note that present theoretical prediction for emergence of antisymmetric diffused mode matches quite well with this experimental observation. The onset shear strains for these instabilities remain nearly independent of the level of confinement. The symmetric diffused modes get activated generally for bulky samples at high stresses, specifically for higher densities.

Strain localization occurs under both rigid and mixed boundary conditions. The onset shear strain for localization is much higher for dense sand in comparison to loose one. The onset shear strain increases but the shear band angle from minor principal direction decreases with the increase in the confining pressure, which is qualitatively in good agreement with the experimental observations of Desrues and Hammad [17], and Han and Drescher [18]. Loading condition has pronounced influence on the instability behavior. Compare to conventional triaxial compression, localized instability modes are more susceptible to emerge in biaxial compression or true triaxial shearing with intermediate stress ratio, $b > 0.4$. The onset strain and shear band orientation angle in biaxial test is very similar to that of true triaxial tests with $b = 0.4$–0.5, which may be due to the similar stress state observed for these two types of test.

Elastic parameters are noticed to have strong impact on both diffused and localized instability onsets. Hence, misinterpretation of elastic properties can significantly influence the instability prediction. As observed from the instability onset charts, void ratio and confinement both have significant effect on the onset shear strain for localization. Whereas, the onset shear strain for diffused instability mainly depends on the relative density of soil.

Table 5
Bifurcation conditions and roots for different diffused instability modes.[a]

Sol.	Roots	Velocity field	Equation of emergence
EI	iZ_1 & iZ_2, $Z_1 = \sqrt{-\widehat{Z}_1}$ $Z_2 = \sqrt{-\widehat{Z}_2}$	x_1-symmetric $V_1(x_1) = A_1 s_1 + B_1 s_2$ $V_2(x_1) = A_2 r_1 + B_2 r_2$	x_1-symmetric $\frac{a_1 Z_1^2 - f}{g Z_1^2 - h} Z_1 t_1 - \frac{a_1 Z_2^2 - f}{g Z_2^2 - h} Z_2 t_2 = 0$
		x_1-antisymmetric $V_1(x_1) = A_1 r_1 + B_1 r_2$ $V_2(x_1) = A_2 s_1 + B_2 s_2$	x_1-antisymmetric $\frac{a_1 Z_1^2 - f}{g Z_1^2 - h} Z_1 l_1 - \frac{a_1 Z_2^2 - f}{g Z_2^2 - h} Z_2 l_2 = 0$
EC	$q \pm ip$, $p = \Im\left(\sqrt{\widehat{Z}_1}\right)$ $q = \Re\left(\sqrt{\widehat{Z}_1}\right)$	$V_1(x_1) = A_1 s_5 r_6 + B_1 r_5 s_6$ $V_2(x_1) = A_2 r_5 r_6 + B_2 s_5 s_6$	$[q s_7 + p s_8](a g (p^2 + q^2)^2 - 2ah (p^2 - q^2) + hf) + [q s_7 - p s_8]$ $(p^2 + q^2)(gf - ah) = 0$
		$V_1(x_1) = A_1 r_5 r_6 + B_1 s_5 s_6$ $V_2(x_1) = A_2 s_5 r_6 + B_2 r_5 s_6$	$[q s_7 - p s_8](a g (p^2 + q^2)^2 - 2ah (p^2 - q^2) + hf) + [q s_7 + p s_8]$ $(p^2 + q^2)(gf - ah) = 0$
P	iZ_1 & Z_2, $Z_1 = \sqrt{-\min\left(\widehat{Z}_1, \widehat{Z}_2\right)}$ $Z_2 = \sqrt{\max\left(\widehat{Z}_1, \widehat{Z}_2\right)}$	$V_1(x_1) = A_1 s_1 + B_1 s_4$ $V_2(x_1) = A_2 r_1 + B_2 r_4$	$\frac{a_1 Z_1^2 - f}{g Z_1^2 - h} Z_1 t_1 + \frac{a_1 Z_2^2 + f}{g Z_2^2 + h} Z_2 t_4 = 0$
		$V_1(x_1) = A_1 r_1 + B_1 r_4$ $V_2(x_1) = A_2 s_1 + B_2 s_4$	$\frac{a_1 Z_1^2 - f}{g Z_1^2 - h} Z_1 l_1 + \frac{a_1 Z_2^2 + f}{g Z_2^2 + h} Z_2 l_4 = 0$
H	Z_1 & Z_2, $Z_1 = \sqrt{\widehat{Z}_1}$ $Z_2 = \sqrt{\widehat{Z}_2}$	$V_1(x_1) = A_1 s_3 + B_1 s_4$, $V_2(x_1) = A_2 r_3 + B_2 r_4$	$\frac{a_1 Z_1^2 + f}{g Z_1^2 + h} Z_1 t_3 - \frac{a_1 Z_2^2 + f}{g Z_2^2 + h} Z_2 t_4 = 0$
		$V_1(x_1) = A_1 r_3 + B_1 r_4$, $V_2(x_1) = A_2 s_3 + B_2 s_4$	$\frac{a_1 Z_1^2 + f}{g Z_1^2 + h} Z_1 l_3 - \frac{a_1 Z_2^2 + f}{g Z_2^2 + h} Z_2 l_4 = 0$

[a] The coefficients used in the Table 5 are defined as follows:

$f = d_3 d_5 - d_4(d_4 + d_7)$, $g = -d_1 d_4$, $h = d_3 d_7$,

$s_1 = \sinh(\beta Z_1 x_1)$, $s_2 = \sinh(\beta Z_2 x_1)$, $s_3 = \sin(\beta Z_1 x_1)$, $s_4 = \sin(\beta Z_2 x_1)$,

$r_1 = \cosh(\beta Z_1 x_1)$, $r_2 = \cosh(\beta Z_2 x_1)$, $r_3 = \cos(\beta Z_1 x_1)$, $r_4 = \cos(\beta Z_2 x_1)$,

$r_5 = \cosh(\beta Z_1 x_1)$, $r_6 = \cosh(\beta Z_2 x_1)$, $r_7 = \cos(\beta Z_1 x_1)$, $r_8 = \cos(\beta Z_2 x_1)$,

$t_1 = \tanh(\beta Z_1 L_1)$, $t_2 = \tanh(\beta Z_2 L_1)$, $t_3 = \tan(\beta Z_1 L_1)$, $t_4 = \tan(\beta Z_2 L_1)$,

$l_1 = \coth(\beta Z_1 L_1)$, $l_2 = \coth(\beta Z_2 L_1)$, $l_3 = \cot(\beta Z_1 L_1)$, $l_4 = \cot(\beta Z_2 L_1)$,

$s_5 = \sinh(\beta p x_1)$, $s_6 = \sin(\beta q x_1)$, $s_7 = \sinh(2\beta p L_1)$, $s_8 = \sin(2\beta q L_1)$,

$r_5 = \cosh(\beta p x_1)$, $r_6 = \cos(\beta q x_1)$,

$\widehat{Z}_1 = \frac{-b_1 + \sqrt{\Delta}}{2a_1}$, $\widehat{Z}_2 = \frac{-b_1 - \sqrt{\Delta}}{2a_1}$.

Appendix A. Governing equations

In absence of body force, the stress rate equilibrium equations of a biaxially loaded drained soil sample of width $2L_1$ and height $2L_2$ can be written in reference configuration as

$$\dot{S}_{11,1} + \dot{S}_{21,2} = 0$$
$$\dot{S}_{12,1} + \dot{S}_{22,2} = 0, \tag{26}$$

where $\dot{\boldsymbol{S}}$ is the true rate of nominal stress tensor. If the current configuration is chosen as the reference configuration, $\dot{\boldsymbol{S}}$ is related to the Jaumann rate of Kirchhoff stress $\overset{\triangledown}{\boldsymbol{\tau}}$ through the Cauchy stress $\boldsymbol{\sigma}$, rate of strain $\boldsymbol{D}$ and spin tensor $\boldsymbol{W}$ by the relation

$$\dot{S}_{ij} = \overset{\triangledown}{\tau}_{ij} - \sigma_{ik} W_{kj} - D_{ik}\sigma_{kj}. \tag{27}$$

The Jaumann rate of Kirchhoff stress $\overset{\triangledown}{\boldsymbol{\tau}}$ can also be expressed in terms of Jaumann rate of Cauchy stress $\overset{\triangledown}{\boldsymbol{\sigma}}$ by the following relation

$$\overset{\triangledown}{\tau}_{ij} = \overset{\triangledown}{\sigma}_{ij} + \sigma_{ij} D_{kk}. \tag{28}$$

In the case of no shear stress, i.e., $\sigma_{12} = \sigma_{21} = 0$, (26)–(28) lead to

$$\overset{\triangledown}{\sigma}_{11,1} + \overset{\triangledown}{\sigma}_{21,2} - (\sigma_{11} - \sigma_{22})W_{12,2} = 0$$
$$\overset{\triangledown}{\sigma}_{12,1} + \overset{\triangledown}{\sigma}_{22,2} - (\sigma_{11} - \sigma_{22})W_{12,2} = 0. \tag{29}$$

Dilation and stresses in tension are considered positive in this analysis.

By combining (27) and (1), the following constitutive relation can be derived

$$\dot{S}_{ij} = \left[C_{ijkl} + \frac{1}{2}(\sigma_{il}\delta_{jk} - \sigma_{jl}\delta_{ik} - \sigma_{jk}\delta_{il} - \sigma_{ik}\delta_{jl}) \right] v_{k,l}, \tag{30}$$

where $\boldsymbol{v}$ is the velocity. For an isotropic material, (29) reduces to the following form after substituting the constitutive relation from (30) and enforcing the kinematic constraint for plane strain loading, i.e., $D_{33} = D_{13} = D_{23} = 0$

$$d_1 v_{1,11} + d_3 v_{1,22} + (d_4 + d_7) v_{2,12} = 0$$
$$d_5 v_{2,11} + d_2 v_{2,22} + (d_4 + d_8) v_{1,12} = 0, \tag{31}$$

where

$$d_1 = C_{1111} - \sigma_{11}, \quad d_2 = C_{2222} - \sigma_{22}$$
$$d_3 = C_{1212} - \frac{1}{2}(\sigma_{11} - \sigma_{22}), \quad d_4 = C_{1212} - \frac{1}{2}(\sigma_{11} + \sigma_{22})$$
$$d_5 = C_{1212} + \frac{1}{2}(\sigma_{11} - \sigma_{22}), \quad d_6 = C_{1212} + \frac{1}{2}(\sigma_{11} + \sigma_{22})$$
$$d_7 = C_{1122}, \quad d_8 = C_{2211}. \tag{32}$$

Appendix B. Diffused instability mode

The bifurcated velocity field corresponding to the diffused instability mode for case-1 (stress controlled) can be represented as

$$v_1(x_1, x_2) = V_1(x_1) \cos(\beta x_2 + \theta_2)$$
$$v_2(x_1, x_2) = V_2(x_1) \sin(\beta x_2 + \theta_2). \tag{33}$$

The coefficients β and θ_2 are selected such that the velocity fields should satisfy the boundary condition given in (10) at $x_2 = \pm L_2$

$$\beta L_2 = \frac{\pi}{2} m \quad \text{for } m = 1, 2, 3, \ldots$$
$$\theta_2 = \begin{cases} 0 & \text{for } m \text{ even} \\ \frac{\pi}{2} & \text{for } m \text{ odd}. \end{cases} \tag{34}$$

The velocity field is x_2-symmetric for even values of m and x_2-antisymmetric for odd values of m. A general form can be assumed for the velocity solutions

$$V_1(x_1) = A e^{i\alpha x_1}$$
$$V_2(x_1) = B e^{i\alpha x_1}, \tag{35}$$

where $i = \sqrt{-1}, \alpha$ is a coefficient and A, B are arbitrary constants. Substituting these velocity fields in (31) and (10), the following characteristic equation can be obtained in terms of the variable $Z = \alpha/\beta$ to get nontrivial solutions for A and B [3]

$$a_1 Z^4 + b_1 Z^2 + c_1 = 0, \tag{36}$$

where

$$a_1 = d_1 d_5, \quad b_1 = d_1 d_2 + d_3 d_5 - (d_4 + d_7)(d_4 + d_8), \quad c_1 = d_2 d_3. \tag{37}$$

Depending on the values of a_1, b_1 and c_1, (36) has four different types of solution in Z:

(EI)   elliptic imaginary when it has four imaginary roots
       ($\Delta \geqslant 0, \quad -b_1/a_1 < 0$ and $c_1/a_1 \geqslant 0$),
(EC)   elliptic complex when it has four complex roots ($\Delta < 0$),
(P)   parabolic when it has two real and two purely imaginary roots ($c_1/a_1 < 0$) and
(H)   hyperbolic when it has four real roots
       ($\Delta = b_1^2 - 4 a_1 c_1 \geqslant 0, \quad -b_1/a_1 \geqslant 0$ and $c_1/a_1 \geqslant 0$).
       Table 5 presents the velocity fields and emergence conditions for each of these type of solutions.

For case-2 with displacement control, the possible diffused instability modes will have the following form in order to satisfy the boundary condition given in (11)

$$v_1 = V_1 \sin(\beta_1 x_1 + \theta_1) \cos(\beta_2 x_2 + \theta_2)$$
$$v_2 = V_2 \cos(\beta_1 x_1 + \theta_1) \sin(\beta_2 x_2 + \theta_2). \tag{38}$$

The coefficients $\beta_1, \beta_2, \theta_1$ and θ_2 satisfy

$$\beta_1 L_1 = \frac{\pi}{2} m_1 \quad \text{for } m_1 = 0, \pm 1, \pm 2, \ldots$$
$$\beta_2 L_2 = \frac{\pi}{2} m_2 \quad \text{for } m_2 = 0, \pm 1, \pm 2, \ldots$$
$$\theta_1 = \begin{cases} 0 & \text{for } m_1 \text{ even} \\ \frac{\pi}{2} & \text{for } m_1 \text{ odd} \end{cases} \quad \text{and} \quad \theta_2 = \begin{cases} 0 & \text{for } m_2 \text{ even} \\ \frac{\pi}{2} & \text{for } m_2 \text{ odd}. \end{cases} \tag{39}$$

The velocity field is x_1-symmetric for even values of m_1 and x_2-symmetric for even values of m_2. Whereas, the odd values of m_1 and m_2 result into x_1-antisymmetric and x_2-antisymmetric velocity fields, respectively. Substitution of velocity field from (38) into (31) and (11) gives the same characteristics equation as (36). Velocity field of the form (38) will exist only in the hyperbolic regime as listed in Table 5.

Appendix C. Localized instability mode

Strain bifurcates into localized modes when a velocity field different from the homogeneous field emerges in a planar region, which is often referred to as shear band [52,7,27]. The velocity continuity condition along with the equilibrium of stress rate across the shear band leads to a characteristic equation for such localization modes [3]

$$a_1 z^4 + b_1 z^2 + c_1 = 0, \tag{40}$$

where $z = n_1/n_2$, $\mathbf{n}$ represents the normal to the shear band and a_1, b_1, c_1 are given in (37). This equation is identical to the characteristic Eq. (36) for diffused bifurcation. As discussed earlier, it has four real solutions in the hyperbolic regime and two real solutions in the parabolic regime (Table 5). The shear band angle (θ_s) from lateral direction (i.e., clockwise from x_1-axis) can be calculated by substituting

$$n_1 = \sin \theta_s \quad \text{and} \quad n_2 = \cos \theta_s. \tag{41}$$

References

[1] Vardoulakis I. Bifurcation analysis of the plane rectilinear deformation on dry sand samples. Int J Solids Struct 1981;17(11):1085–101.
[2] Vardoulakis I. Stability and bifurcation of undrained, plane rectilinear deformations on water-saturated granular soils. Int J Numer Anal Meth Geomech 1985;9:399–414.
[3] Bardet JP. Analytical solutions for the plane-strain bifurcation of compressible solids. J Appl Mech 1991;58:651–7.
[4] Bardet JP, Shiv A. Plane-strain instability of saturated porous media. J Eng Mech 1995;121:717–24.
[5] Vardoulakis I, Sulem J. Bifurcation analysis in geomechanics. London, UK: Chapman and Hall publ.; 1995.
[6] Iai S, Bardet JP. Plane strain instability of saturated elasto-plastic soils. Geotechnique 2001;51(5):389–98.
[7] Vardoulakis I, Goldscheider M, Gudehus G. Formation of shear bands in sand bodies as a bifurcation problem. Int J Numer Anal Meth Geomech 1978;4:99–128.
[8] Vardoulakis I. Bifurcation analysis of the triaxial test on sand samples. Acta Mech 1979;32:35–54.
[9] Han C, Vardoulakis I. Plane strain compression experiments on water saturated fine grained sand. Geotechnique 1991;41(1):49–78.
[10] Finno RJ, Harris WW, Mooney MA, Viggiani G. Shear bands in plane strain compression of loose sand. Geotechnique 1997;47(1):149–65.
[11] Lade PV. Instability, shear banding, and failure in granular materials. Int J Solids Struct 2002;39:3337–57.
[12] Desrues J, Viggiani G. Strain localization in sand: an overview of the experimental results obtained in Grenoble using stereophotogrammetry. Int J Numer Anal Meth Geomech 2004;28(4):462–73.
[13] Chu J, Wanatowski D. Effect of loading mode on strain softening and instability behavior of sand in plane-strain tests. J Geotech Geoenviron Eng 2009;135 (1):108–20.
[14] Desrues J, Lanier J, Stutz P. Localization of the deformation in tests on sand sample. Eng Fract Mech 1985;21(4):909–21.
[15] Peters JF, Lade PV, Bro A. Shear band formation in triaxial and plane strain tests. Advanced Triaxial Testing of Soil and Rock, ASTM STP, 977, 1988. p. 604–27.
[16] Alshibli KA, Batiste SN, Sture S. Strain localization in sand: plane strain versus triaxial compression. J Geotech Geoenviron Eng 2003;129(6):483–94.

[17] Desrues J, Hammad W. Shear banding dependency on mean stress level in sand. In: Dembicki E, Gudehus G, Sikora Z, editors. 2nd international workshop on numerical methods for localization and bifurcation of granular bodies, Gdansk-Karlsruhe. p. 57–67.

[18] Han C, Drescher A. Shear bands in biaxial tests on dry coarse sand. Soils Found 1993;33(1):118–32.

[19] Daouadji A, AlGali H, Darve F, Zeghloul A. Instability in granular materials: experimental evidence of diffuse mode of failure for loose sands. J Eng Mech 2010;136(5):575–88.

[20] Wan R, Pinheiro M, Daouadji A, Jrad M, Darve F. Diffuse instabilities with transition to localization in loose granular materials. Int J Numer Anal Meth Geomech 2013;37:1292–311.

[21] Lignon S, Laouafa F, Prunier F, Khoa H, Darve F. Hydromechanical modelling of landslides with a material instability criterion. Geotechnique 2009;59 (6):513–24.

[22] Wan RG, Pinheiro M, Guo PJ. Elastoplastic modelling of diffuse instability response of geomaterials. Int J Numer Anal Meth Geomech 2011;35: 140–60.

[23] Chu J, Leong WK, Loke WL, Wanatowski D. Instability of loose sand under drained conditions. J Geotech Geoenviron Eng 2012;138(2):207–16.

[24] Hill R, Hutchinson JW. Bifurcation phenomena in the plane tension test. J Mech Phys Solids 1975;23:239–64.

[25] Young NJB. Bifurcation phenomena in plane compression test. J Mech Phys Solids 1976;24:77–91.

[26] Needleman A. Non-normality and bifurcation in plane-strain tension and compression. J Mech Phys Solids 1979;27(3):231–54.

[27] Vardoulakis I. Shear band inclination and shear modulus of sand in biaxial tests. Int J Numer Anal Meth Geomech 1980;4:103–19.

[28] Chau KT, Rudnicki JW. Bifurcation of compressible pressure-sensitive materials in plane strain tension and compression. J Mech Phys Solids 1990;38(6):875–98.

[29] Gajo A, Bigoni D, Wood DM. Multiple shear band development and related instabilities in granular materials. J Mech Phys Solids 2004;52:2683–724.

[30] Gajo A, Wood DM, Bigoni D. On certain critical material and testing characteristics affecting shear band development in sand. Gotechnique 2007;57:449–61.

[31] Mukherjee M, Gupta A, Prashant A. Instability analysis of sand under undrained biaxial loading with rigid and flexible boundary. Int J Geomech, http://dx.doi.org/10.1061/(ASCE)GM.1943-5622.0000690.

[32] Truesdell C, Noll W. Nonlinear field theories of mechanics. Handbuch of physics, III/3. New York, USA: John Wiley and Sons; 1965.

[33] Atluri SN. On some new general and complementary energy theorems for the rate problems in finite strain, classical elastoplasticity. J Struct Mech: Int J 1980;8(1):61–92.

[34] Reed KW, Atluri SN. Constitutive modeling and computational implementation for finite strain plasticity. Int J Plast 1985;1:63–87.

[35] Gurtin M, Fried E, Anand L. The mechanics and thermodynamics of continua. UK: Cambridge University Press; 2010.

[36] Wood DM. Geotechnical modeling. Floria, USA: Taylor and Francis group, CRC Press; 2004.

[37] Desai CS, Siriwardane HJ. Constitutive laws for engineering materials: with emphasis on geologic materials. USA: Prentice-Hall; 1984.

[38] Lade PV, Nelson RB. Modelling the elastic behavior of granular materials. Int J Numer Anal Meth Geomech 1987;11:521–42.

[39] Hicher PY. Elastic properties of soils. J Geotech Eng 1996;122(8):641–8.

[40] Houlsby GT, Amorosi A, Rojas E. Elastic moduli of soils dependent on pressure: a hyperelastic formulation. Geotechnique 2005;55(5):383–92.

[41] Einav I, Puzrin AM. Pressure-dependent elasticity and energy conservation in elastoplastic models for soils. J Geotech Geoenviron Eng 2014;130(1):81–92.

[42] Gajo A, Wood DM. A kinematic hardening constitutive model for sands: the multiaxial formulation. Int J Numer Anal Meth Geomech 1999;23:925–65.

[43] Hardin BO, Black WL. Sand stiffness under various triaxial stresses. J Soil Mech Found Eng Div, ASCE 1966;91(SM2):353–69.

[44] Simo JC, Hughes TJR. Computational inelasticity. New York, USA: Springer; 2000.

[45] Dodds RH, Healy BE. A large strain plasticity model for implicit finite element analyses. Tech. Rep. UILU-ENG-91-2001, Urbana, Illinois: University of Illinois at Urbana-Champaign, Department of Civil Engineering; 2001.

[46] Hill R. A general theory of uniqueness and stability in elastic-plastic solids. J Mech Phys Solids 1958;5:236–49.

[47] Bigoni D. Bifurcation and instability of nonassociative elasticplastic solids. In: Petryk H, editor. Material instabilities in elastic and plastic solids. CISM Lecture Notes, vol. 414. New York, USA: Springer-Verlag; 2000. p. 1–52.

[48] Bigoni D. Nonlinear solid mechanics bifurcation theory and material instability. UK: Cambridge University Press; 2012.

[49] Raniecki B. Uniqueness criteria in solids with non-associated plastic flow laws at finite deformation. Bull Polish Acad Sci 1979;27(8–9):391–9.

[50] Raniecki B, Bruhns OT. Bounds to bifurcation stresses in solids with non-associated plastic flow law at finite strain. J Mech Phys Solids 1981;29 (2):153–72.

[51] van Hove L. Sur lextension de la condition de Legendre du calcul des variations aux integrales multiples a plusieurs fonctions inconnues. Proc Kon Ned Akad Wet 1947;50:18–23.

[52] Rudnicki JW, Rice JR. Conditions for the localization of deformation in pressure-sensitive dilatants materials. J Mech Phys Solids 1975;23:371–94.

[53] Bardet JP. A comprehensive review of strain localization in elastoplastic soils. Comput Geotech 1990;10:163–88.

[54] Arthur JFR, Dunstan T, Assadi QAJ, Assadi A. Plastic deformation and failure in granular material. Geotechnique 1977;27:53–74.

[55] Rice JR. The localization of plastic deformation. Theoretical and applied mechanics, proc.of the 14th int. cong. on theoretical and applied mechanics, Delft, vol. 1. p. 207–20.

[56] Lade PV, Wang Q. Analysis of shear banding in true triaxial tests on sand. J Eng Mech 2001;127(8):762–8.

[57] Wang Q, Lade P. Shear banding in true triaxial tests and its effect on failure in sand. J Eng Mech 2001;127(8):754–61.